The International Journal of Advanced Manufacturing Technology (2019) 102:2063–2083
https://doi.org/10.1007/s00170-019-03302-3

ORIGINAL ARTICLE

Weld process model for simulating metal active gas welding

Dénes Kollár[1] · Balázs Kövesdi[1] · László Gergely Vigh[1] · Sándor Horváth[2]

Received: 30 September 2018 / Accepted: 4 January 2019 / Published online: 19 January 2019

Abstract
Generally, optimum welding variables and conditions of manufacturing are currently mainly determined by experiments for standardized production. Virtual manufacturing and virtual testing of weldments using finite element method provide a sustainable solution for advanced applications. The aim of the current research work is to develop a weld process model, using a three-dimensional heat transfer model, to ensure general applicability for typical joints of stator segments of wind turbines as a final application. A systematic experimental research program, containing temperature measurements during welding, macrographs, and deformation measurements, is carried out on small-scale test specimens using different welding variables. In addition, a numerical study using uncoupled transient thermomechanical analysis is performed. The weld process model uses Goldak's double ellipsoidal heat source model for a metal active gas welding power source. It describes the correspondence between heat source parameters and net heat input for two types of electrodes. The model is validated via cross-sectional areas of fusion zones and deformations based on experiments. The relationship between current and voltage is determined based on large number of experimental data; thus, selecting a wire type, travel speed, and voltage directly defines the heat source parameters of the weld process model.

Keywords Welding simulation · Heat source model · Validation · Metal active gas welding · Numerical simulation · Weld process model

1 Introduction

There is a remarkable industrial demand on speeding up and improving manufacturing processes. Lindgren [1] revealed that welding technologies are generally developed by performing experiments and tests on prototypes, while computational methods are still rarely used in the development process. It is a substantial expectation that simulations will complement experiments using the "trial and error" process for obtaining Welding Procedure Specifications as a final result. Namely, both residual stresses and deformations are evaluated in the design phase to optimize welded structures. However, nowadays, deformations are usually in focus whereas residual stresses are of interest in subsequent phases.

In most of the cases, it is time efficient and economical to use computer-aided engineering opportunities rather than determining optimal parameters experimentally. Developing a sustainable virtual manufacturing process is an innovative way to reduce waste in workshops and specify optimal conditions depending on the requirements. Goldak and Akhlaghi [2] denoted that in the automotive industry the number of prototypes has been reduced from a dozen to one or two applying computer-aided engineering sources as powerful, robust, and efficient tools. The general aim of computational welding mechanics is to set up reasonably precise methods and models that are capable of controlling and designing welding technologies whilst ensuring suitable performance [3]. Obviously, it is an overall aim to perform numerical simulations faster and easier than to carry out welding experiments, especially when dealing with large welded structures [4]. The welding simulation procedure can be implemented in full-scale modeling frameworks describing the entire manufacturing process including steel rolling, cold forming, thermal cutting, and machining [5]. An additional tremendous

✉ Dénes Kollár
kollar.denes@epito.bme.hu

[1] Department of Structural Engineering, Budapest University of Technology and Economics, 3 Műegyetem rakpart, Budapest H-1111, Hungary

[2] Lakics Machine Manufacturing Ltd., 1 Izzó utca, Kaposvár H-7400, Hungary

advantage of computational welding mechanics is comparing different variants in the design phase, while performing subsequent analyses on virtual specimens, such as buckling [6–8] or fatigue analysis, is also a potential.

The determination of residual stresses and deformations is highly recommended for manufacturers as well as for designers. In the case of steel structures, there are often assembly difficulties and resistance problems due to large weld sizes, high heat inputs, or poor clamping conditions during manufacturing. These effects can result in large deformations and residual stresses, which can reduce the resistance of steel structural elements. Most of the standards, such as EN 1993-1-5:2005 [9], give only approximations for the equivalent (or initial) geometrical imperfections. Nowadays, due to the improvement of hardware and computational approaches, it is feasible to examine large-scale welded joints and structures in an adequately accurate way, but it has to be declared that computations still have boundaries.

The aim of the current research is to develop a weld process model based on Goldak's double ellipsoidal heat source model. A systematic research program is carried out on small-scale specimens using different welding variables. The experimental research program contains temperature measurements during welding, macrographs, and deformation measurements after welding. In addition, a numerical study using transient thermomechanical analysis is performed. The research program focuses on the relationship of welding variables and heat source model parameters. Based on the large number of experimental data, e.g., fusion zone size and deformations, thermal efficiency and heat source model parameters are calibrated and verified. The weld process model provides the heat source parameters as a function of net heat input. The validated model is able to increase structural performance of welded joints, while reducing the need of further experiments in the workshop of steel manufacturer companies, such as in the case of the project partner, Lakics Machine Manufacturing Ltd. The validation procedure can be used by other researchers as well, while the validated heat source parameters are applicable for a metal active gas welding power source and two electrode types. The developed validation process can have significant role in the case of robotic welding, where welding trajectory, heat input, travel speed, and quality can be controlled precisely.

2 Literature review

Experiments and measurements are intended to assist in getting acquainted with heat sources. There is a fundamental need for better understanding the influence of certain parameters and more precise approaches to predict the realistic behavior during welding. Mathematical models are used to enhance the knowledge of heat sources taking distinct effects into account. Generally, the aim is to model the heat source as accurate as it is necessary depending on one's purpose. Therefore, Goldak and Akhlaghi [2] classified five generations of weld heat source models. The fifth class is the newest and most complex. The older ones are considered as subclasses of each newer generation as latter generations include the attributes of former models. Table 1 sums up the pros, cons, applicability, and the need for calibration of each weld heat source model generation. The literature review focuses on the second-generation weld heat source models as these are relevant for the presented finite element calculations. Heat source models can be generalized for welding processes in a parameter range. According to Lindgren [3], weld process models are coupling the physics of the problem, the power density distribution in the weld pool and welding process parameters. Sudnik et al. [10, 11] set up such a model earlier for laser beam welding taking energy transport, vapor pressure, and capillary pressure as well into account. Weld process models have much importance as experiments can be combined or fully replaced by calibrated heat source models in the region of interest [12].

First-generation heat sources comprehend point, line, and plane heat source models. The development of instantaneous point heat source models for two- and three-dimensional heat flow, solving the heat flow differential equation for quasi-stationary state, is credited to Rosenthal [13] and Rykalin [14]. Rosenthal made a few assumptions such as (i) the energy input from the heat source is uniform and moves with a constant velocity along a trajectory; (ii) all the energy is deposited into the weld at a single point; (iii) thermal properties are temperature-independent; (iv) heat flow is governed by conduction, meanwhile radiation and convection are ignored; and (v) in addition, latent heats due to phase transformations and fusion/solidification are neglected. The temperature field far from the weld bead could be determined with acceptable accuracy, but the precision of these analytical approaches may decrease severely in the fusion zone and the heat-affected zone. On the other hand, quasi-stationary state may not even exist for welded structures with complex welding trajectories according to Goldak et al. [15]; thus, the utilization of first-generation weld heat source models is restricted.

Second-generation weld heat source models define distribution functions instead of solving Dirichlet problems of first-generation models. It is mainly applied in finite element analysis and is suitable to handle complex geometries, weld pool shapes, and welding trajectories, while temperature-dependent material properties, radiation and convection, phase transformations, and latent heats due to phase transformations, fusion, and evaporation can be taken into account. These models have to fulfill solely the heat equation; thus, power density, prescribed flux, and prescribed temperature functions are in this class according to [2, 16]. The first innovative conception was a distributed flux model developed by

Table 1 Pros, cons, applicability, and the need for calibration of weld heat source model generations (WHSMG)

WHSMG	Pros	Cons	Applicability/calibration
First	Analytical solution Low computational cost	Distribution of energy ☒ Constant material properties Phase transformations ☒ Radiation and convection ☒ Simple weldment geometry Straight weld path Discontinuities in geometry ☒ Constant travel speed Quasi-steady state heat transfer	Approximates temperature for finite, infinite, or semi-infinite bodies without discontinuities and nonlinearities Supports optimizing welding variables Makes approximations on phase proportions and hardness possible Calibration is not really possible
Second	Distribution of energy Nonlinear material properties Phase transformations Radiation and convection Complex weld path Complex weldment geometry Discontinuities in geometry Varying travel speed Unsteady state heat transfer Moderate computational cost	Fluid flow ☒ Complex weld pool shapes ☒/☑	FDM or FEM: handles nonlinearities Realistic temperature fields outside of the weld pool Complex weld pool shapes using prescribed temperature model or combination of surface and/or volumetric heat source models Calibration is needed
Third	Stefan problem Cauchy momentum equation Complex weld pool shapes Higher computational cost	Additional input data may be needed for pressure distribution of the arc, mass flow rate into the weld pool, and surface tension on the liquid surface	Can take welding positions into account Weld pool shape becomes output data Calibration is not needed
Fourth	Fluid dynamics Complex weld pool shapes	Mathematical difficulties High computational cost	FVM: droplet flow can be included; Calibration is not needed
Fifth	Model of the arc is included Magneto-hydrodynamics Complex weld pool shapes	Mathematical difficulties High computational cost	Most general heat source model generation Application is actually limited to researches Calibration is not needed

FDM, finite difference method; *FEM*, finite element method; *FVM*, finite volume method

Pavelic et al. [17] and Rykalin [18] to model weld pools without nail-head shape or deep penetration. The description of distributed flux models, e.g., normal Gaussian distributed surface heat source and bivariate Gaussian distributed surface heat source, is given in [2] in a detailed manner. Prescribed temperature model was used by, e.g., [19, 20]. Goldak, Chakravarti, and Bibby [21] presented power density functions to model even complex weld pool shapes for arc welding or laser beam welding. General power density functions of spherical, hemispherical, single ellipsoidal, and double ellipsoidal heat sources are gathered in [2, 16] as well. Recently, hybrid heat source models [22–25] are also published, as combination of heat source models is feasible for non-conform cases.

The current paper uses Goldak's double ellipsoidal heat source model, a second-generation weld heat source model, as a basis of weld process model development. The weld process model provides the parameters of the double ellipsoidal heat source as a function of net heat input. According to the authors' knowledge, such a weld process model has not been published yet. The validated model is applicable to a metal active gas welding power source and two electrode types. The aim is to increase structural performance of welded joints, while reducing the need for further experiments in the workshop of steel manufacturer companies. A three-dimensional heat transfer model is used to ensure general applicability for typical joints of stator segments of wind turbines as a final application.

3 Experimental research program

Small-scale welded T-joints (Fig. 1) of a stator segment of a wind turbine are investigated in the current study. The major aim of the experimental research program is to evaluate the effects of different filler metals, welding variables, and types of welding joints on productivity and structural behavior. High-cycle fatigue is crucial in the case of wind turbines; therefore, three types of joints are analyzed (Fig. 2) having considerably different resistance against cyclic loading: (a) double-bevel butt weld, (b) double-sided fillet welds, and (c) single-bevel butt weld.

A number of weld passes and heat input per unit length are the investigated variables resulting in a database of input parameters including the cross-sectional area of the fusion zones. Fusion zone size is measured after fabrication using

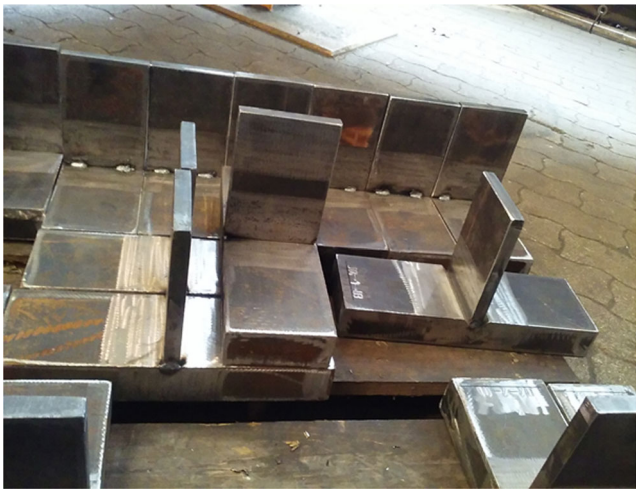

Fig. 1 Tack welded T-joints before welding

macrographs and it is considered to be the basis of the heat source model validation process. The initial and deformed configurations of the joints are measured with a coordinate-measuring machine at specific points, denoted by M1–M8 in Fig. 2; thus, welding-induced deformations can be calculated after using common coordinate transformations. Vickers hardness tests, microstructural analyses, and temperature measurements during welding are also carried out. Thirty welded specimens are manufactured altogether. The following notations are used for the joints (e.g., JT*X*-*Y*-0*Z*): JT—T-joint; *X*—1/2/3—double-bevel butt weld with bevel angles of 45° and a root gap of 3 mm/double-sided fillet welds/single-bevel butt weld with a bevel angle of 45°; *Y*—1/2—solid wire/flux cored electrode; *Z*—number of specimen. All the specimens have a length of 100 mm. Base plates are manufactured from steel plates with dimensions of 300 × 100 × 40 mm^3, while stiffeners have dimensions of 140 × 100 × 15 mm^3. Plasma cutting is used for carving the plates. Steel grade is S355J2+N for base plates and stiffeners as well; the chemical composition is summed up in Table 2 according to the inspection certificate.

A Fronius TransPuls Synergic 5000 welding power source, M21 - ArC - 18 (Corgon 18) shielding gas, and PA flat or PB horizontal-vertical welding positions are used for metal active gas (MAG) welding. Solid wire (Esab OK Aristorod 12.50) and flux cored (Böhler Ti52 T-FD) electrodes with diameters of 1.2 mm are used during manufacturing. Preheat and interpass temperatures are both 150 °C. Ambient temperature is between 20 and 22 °C during the experiments. The total heat input per unit length varies between 0.60 and 2.71 kJ/mm depending on filler metal, joint type, and number of passes. Welding sequences are shown in Figs. 3 and 4 for all the specimens, while Tables 3, 4, 5, and 6 sum up specimen notations; number of weld pass #; type of filler metal; welding current *I*; voltage *U*; travel speed *v*, denoting (+) positive and (−) negative welding directions; total heat input per unit length $q = UI/v$, fusion zone size A_{FZ} based on measurements using macrographs (Figs. 5, 6, 7, and 8); and maximum measured transverse deformation $U_{x,max}$, respectively. Fusion zone sizes in the tables are related to the whole joint in several cases as multi-pass welding is used for multiple weldments. Welding variables, such as voltage, current, and travel speed, are registered during welding; therefore, total heat input per unit length can be calculated. Three of the double-bevel butt weld configurations are welded only on single side; however, these joints are also listed under the corresponding tables and the macrographs are shown in the corresponding figures.

The deformations due to welding differ in a great extent in the case of the presented types of joints, as the number of weld passes, total heat input, and single/double-sided welding have a large influence on residual strains. The most important component of deformations is the transverse deformation of the top due to angular distortion; the base plates are much stiffer; thus, vertical deformations are quasi-zero. Maximum transverse deformations $U_{x,max}$ and the cross-sectional area of the fusion zone A_{FZ} for every single case are shown in Fig. 9; measurements are sorted in groups regarding the types of the joints. A linear regression analysis is carried out using the least squares method to determine the relationship between A_{FZ} and the total heat input per unit length $q = UI/v$, marked by continuous solid lines, for double-sided fillet welds with single weld passes. Measurements and derived heat input data are showed in Fig. 9 as well. Error bars are denoting the standard deviation of discrepancies ($s = 7.58$ mm^2 and 3.95 mm^2 for solid wire and flux cored electrodes, respectively) between measured data and corresponding values of the regression line due to uncertainties in welding variables as arc length and travel speed are not constant during welding. Nevertheless, the slopes of continuous lines are different, which means that the size of fusion zone is smaller in the case of flux cored

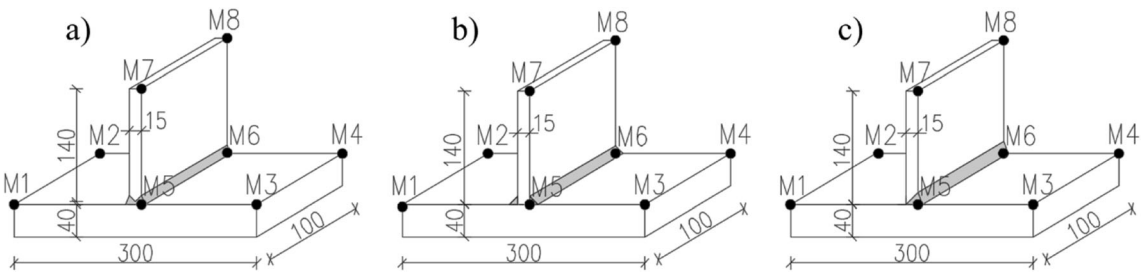

Fig. 2 Types of investigated joints: **a**) double-bevel butt weld, **b**) double-sided fillet welds, and **c**) single-bevel butt weld

Table 2 Chemical composition of S355J2+N according to inspection certificate

C%	Mn%	Si%	S%	P%	Cr%	Ni%	Al%	Cu%	Mo%	Nb%	V%	Ti%	N%
0.164	1.295	0.188	0.003	0.010	0.017	0.012	0.039	0.018	0.001	0.020	0.002	0.001	0.0038

electrodes by using the same total heat input per unit length. Different thermal efficiencies and the protective slag formed over the weld, which is removed when using flux cored electrodes, may be an explanation of the discrepancies.

Maximum transverse deformations at the top of the specimens are evaluated regarding the joint type and the cross-sectional area of the fusion zone. Specimen JT3-1-03 with single-bevel butt weld (SBBW) has not been taken into account in the assessment process as tack welds have fractured during transportation. The plates are repositioned and new tack welds are laid; therefore, the measurements of the deformed configuration cannot be used for deformation calculations. In addition, JT1-2-01, JT1-2-02, and JT1-2-03 T-joints are manufactured with single-bevel butt welds instead of double-bevel butt welds (DBBW); hence, they are treated as JT3 specimens. An obvious trend cannot be determined in the case of multi-pass welding of double-sided fillet welds (DSFW-M) and double-bevel butt welds due to insufficient data. Larger transverse deformations and heat inputs are characteristic for larger fusion zones in the case of joints with double-sided fillet welds with single weld passes (DSFW-S) regarding the whole joint.

Temperature is measured by a thermocouple and an infrared thermal camera during welding. The camera uses a fixed value for emissivity; therefore, a code is developed to calibrate the measurements of the camera using data recorded by the thermocouple. The measurement range of Type K (Chromel/Alumel) thermocouples is − 200–1200 °C, while the sensitivity is around 41 μV/°C. Thermoelectric voltages are converted to temperatures via a Thermo-MXBoard thermocouple adapter and a QuantumX MX840A data acquisition system, which operates as a universal amplifier. The temperature variation in time is plotted; therefore, real-time monitoring of fixed points is possible during experiments. A ThermoPro™ TP8S infrared thermal camera with high-temperature filter is part of the measurement system as well. It uses a focal plane array uncooled microbolometer with 384 × 288 pixels. Its spectral range is 8–14 μm, while its sensitivity is 0.08 °C at 30 °C. The measurement range is − 200–2000 °C, while the operating temperature is between − 20 and 60 °C. The measured virtual temperatures (by the infrared thermal camera) are calibrated according to thermocouple measurements; thus, a temperature scaling is necessary. The principle of scaling is having the same computed areas under the curves, provided by the infrared camera at the same location as the thermocouple; thereunto, trapezoidal rule integration is used. Surface and material properties could be handled easily, while the temperature-dependent emissivity is also taken into consideration.

Thermal cycles are determined for three specimens (JT1-2-01, JT1-2-02, and JT1-2-03) using a thermocouple located 15 mm far from the stiffener in transverse direction and positioned in the midsection longitudinally. Virtual temperatures of the infrared camera are calibrated according to thermocouple measurements via temperature scaling for different temperature ranges. Figure 10 shows temperature measurements for a specimen, while error bars are denoting the $s = 20.6$ °C standard deviation of temperature differences derived from the two approaches. Hereafter, temperature scaling factors can be applied at arbitrary points for further weldments when the infrared thermal camera is used.

Vickers hardness tests and microstructural analyses are also carried out for six specimens (two for each type of welding joint). A ferritic and pearlitic microstructure is specific for the base material; its hardness varies between 153 and 173 HV. The highest hardness values are measured at the boundary of the heat-affected zone and the fusion zone; the maximum values are between 253 and 363 HV. A significant decrease of 30–110 HV can be observed in the fusion zone. The fusion zone contains ferrite, pearlite, and bainite, while a ferritic and pearlitic microstructure is typical for the heat-affected zone

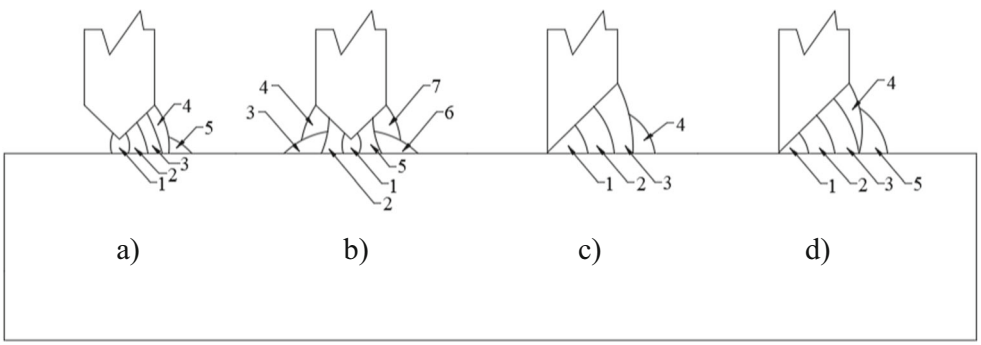

Fig. 3 Welding sequences for **a**)–**b**) double-bevel and **c**)–**d**) single-bevel butt welds

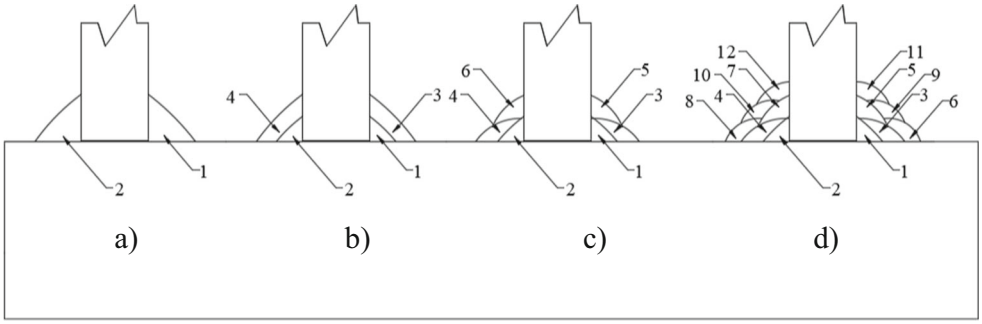

Fig. 4 Welding sequences for **a**) single-pass and **b**)–**d**) multi-pass welding of double-sided fillet welds

Table 3 Welding variables, size of fusion zone, and maximum transverse deformation for double-bevel butt welds

Specimen	#	Filler metal	I (A)	U (V)	v (mm/s)	q (kJ/mm)	A_{FZ} (mm^2)	$U_{x,max}$ (mm)
JT1-1-01	1	Solid wire	190	17.6	+ 5.56	0.60	313	2.80
	2	Solid wire	281	28.5	+ 5.00	1.60		
	3	Solid wire	294	28.5	+ 5.26	1.59		
	4	Solid wire	269	27.7	+ 5.26	1.42		
	5	Solid wire	280	28.8	− 3.33	2.42		
	6	Solid wire	280	28.8	− 4.35	1.85		
	7	Solid wire	270	27.8	− 5.56	1.35		
JT1-1-02	1	Solid wire	190	18.6	+ 4.35	0.81	323	3.09
	2	Solid wire	187	18.5	+ 4.76	0.73		
	3	Solid wire	246	25.1	+ 5.56	1.11		
	4	Solid wire	270	27.8	+ 5.00	1.50		
	5	Solid wire	280	28.8	− 3.70	2.18		
	6	Solid wire	280	28.8	− 5.00	1.61		
	7	Solid wire	270	27.8	− 5.26	1.43		
JT1-1-03	1	Solid wire	190	18.6	+ 3.57	0.99	331	2.80
	2	Solid wire	281	28.8	+ 4.55	1.78		
	3	Solid wire	280	29.1	+ 5.26	1.55		
	4	Solid wire	270	27.8	+ 5.26	1.43		
	5	Solid wire	280	28.8	− 3.33	2.42		
	6	Solid wire	280	28.8	− 4.17	1.93		
	7	Solid wire	270	27.8	− 5.56	1.35		
JT1-2-01	1	Flux cored	240	22.8	+ 4.17	1.31	150	7.50
	2	Flux cored	260	23.5	+ 4.35	1.40		
	3	Flux cored	250	23.3	− 4.76	1.22		
	4	Flux cored	240	23.1	+ 5.00	1.11		
	5	Flux cored	240	23	− 5.26	1.05		
JT1-2-02	1	Flux cored	260	23.5	+ 3.85	1.59	171	7.89
	2	Flux cored	240	22.7	+ 4.00	1.36		
	3	Flux cored	240	22.7	− 3.85	1.42		
	4	Flux cored	240	22.7	− 4.55	1.20		
	5	Flux cored	240	22.7	− 4.00	1.36		
JT1-2-03	1	Flux cored	250	23	+ 4.55	1.26	152	7.83
	2	Flux cored	260	23.2	+ 4.55	1.33		
	3	Flux cored	260	23.2	+ 5.00	1.21		
	4	Flux cored	260	23.2	+ 5.88	1.03		
	5	Flux cored	260	23.2	+ 5.56	1.08		

Table 4 Welding variables, size of fusion zone, and maximum transverse deformation for double-sided fillet welds (single-pass welding)

Specimen	#	Filler metal	I (A)	U (V)	v (mm/s)	q (kJ/mm)	A_{FZ} (mm^2)	$U_{x,max}$ (mm)
JT2-1-01	1	Solid wire	270	28.5	+4.00	1.92	69	3.35
	2	Solid wire	270	28.5	−4.00	1.92	74	
JT2-1-02	1	Solid wire	221	20.6	+2.13	2.14	61	0.46
	2	Solid wire	221	20.6	−2.32	1.96	59	
JT2-1-03	1	Solid wire	315	29.6	+4.17	2.24	85	2.35
	2	Solid wire	315	30.3	−4.55	2.10	85	
JT2-1-04	1	Solid wire	239	23.5	+3.70	1.52	55	1.36
	2	Solid wire	229	23.5	−3.33	1.62	50	
JT2-1-05	1	Solid wire	280	28.4	+4.00	1.99	71	1.60
	2	Solid wire	261	28.5	−3.85	1.93	68	
JT2-1-06	1	Solid wire	305	29.7	+4.77	1.90	75	1.87
	2	Solid wire	280	29.7	−4.17	1.99	74	
JT2-2-01	1	Flux cored	282	22.9	+2.92	2.21	67	0.72
	2	Flux cored	282	22.9	−4.00	1.61	56	
JT2-2-02	1	Flux cored	210	20.9	+2.94	1.49	43	1.82
	2	Flux cored	210	20.5	−3.33	1.29	39	
JT2-2-03	1	Flux cored	311	23.7	+5.00	1.47	45	0.60
	2	Flux cored	311	24	−5.00	1.49	47	
JT2-2-04	1	Flux cored	265	23.6	+4.17	1.50	41	0.58
	2	Flux cored	265	23.6	−4.35	1.44	44	
JT2-2-05	1	Flux cored	232	22.5	+3.57	1.46	38	0.66
	2	Flux cored	232	22.5	−3.70	1.41	43	
JT2-2-06	1	Flux cored	311	23.9	+4.55	1.63	51	0.88
	2	Flux cored	270	23.3	−4.17	1.51	49	

with bainitic patterns in some cases. Cooling rate is lower in the weld pool and on its surface than in the heat-affected zone. The so-called $\Delta t_{8/5}$ cooling time, which is necessary for cooling from 800 to 500 °C, has to be shorter for the base plate as higher hardness values are measured, in the corresponding heat-affected zone, than in the stiffener. There is no significant difference in hardness between face and root side, except in the case of single-bevel butt welds naturally. The type of filler metal does not have any notable influence on hardness in these cases. Hardness profiles of double-sided fillet welds do not differ in a great extent. Hardness profiles of JT2-1-01 for face and root sides and the points used for measurements are presented in Fig. 11.

The weldments are manufactured by using a Fronius TransPuls Synergic 5000 welding power source for MAG welding using constant voltage (slightly drooping) characteristics. Direct current and reverse polarity (DC+) are applied for the current applications. Welding current (I) and voltage (U) are registered during welding; thus, the operating points for each weld pass, assuming that arc length is constant, can be determined for configurations with solid wire and flux cored electrodes as arc characteristics for different filler metals, wire diameters, and shielding gases are distinct. The solid wire electrode is an Esab OK Aristorod 12.50 (EN ISO 14341-A G 42 4 M G3Si1) and the flux cored electrode is a Böhler Ti52 T-FD (EN ISO 17632-A T 46 4 P M 1 H5). The diameter of electrodes is 1.2 mm, while shielding gas is EN ISO 14175 - M21 - ArC – 18 and gas flow rate is 12–15 l/min. Eighty-two weld passes are laid using solid wire electrodes and 81 weld passes are carried out applying flux cored electrodes; hence, the number of data points is equal to the number of weld passes in Fig. 12. A linear regression analysis is carried out using the least squares method to determine the welding current-voltage relationship for globular and spray arc metal transfer modes, marked with continuous solid lines, for both electrodes. Error bars are denoting standard deviations of discrepancies ($s = 0.81$ V and $s = 0.38$ V), for solid wire and flux cored electrodes, between measured data and corresponding values of the regression line representing the uncertainties in arc characteristic ranges, i.e., increase and decrease of contact tip-to-workpiece distance and arc length.

The current-voltage equations of the solid lines for the solid wire and flux cored electrodes are

$$U_{\text{solid}}(I) = 0.103I - 0.45 \tag{1}$$

$$U_{\text{flux}}(I) = 0.02318I + 17 \tag{2}$$

representing the operating points after the linear regression analysis. These equations can be applied in the preliminary design phase when calculating heat input. In addition, they are implemented in the numerical model developed for the welding simulation of T-joints.

Table 5 Welding variables, size of fusion zone, and maximum transverse deformation for double-sided fillet welds (multi-pass welding)

Specimen	#	Filler metal	I (A)	U (V)	v (mm/s)	q (kJ/mm)	A_{FZ} (mm^2)	$U_{x,max}$ (mm)
JT2-1-07	1	Solid wire	278	27.9	+ 8.33	0.93	94 + 95	1.53
	2	Solid wire	262	27.9	+ 7.69	0.95		
	3	Solid wire	276	27.8	− 3.85	1.99		
	4	Solid wire	278	27.8	− 3.45	2.24		
JT2-1-08	1	Solid wire	276	28.3	+ 6.67	1.17	114 + 125	1.63
	2	Solid wire	257	28.2	+ 6.67	1.09		
	3	Solid wire	267	28.2	− 5.88	1.28		
	4	Solid wire	277	27.4	− 6.25	1.21		
	5	Solid wire	262	26.5	+ 5.56	1.25		
	6	Solid wire	259	26.5	− 5.56	1.23		
JT2-1-09	1	Solid wire	274	28.1	+ 6.67	1.15	193 + 197	0.99
	2	Solid wire	269	28.5	+ 7.14	1.07		
	3	Solid wire	265	26.9	− 7.69	0.93		
	4	Solid wire	262	27	− 7.14	0.99		
	5	Solid wire	260	26.2	+ 6.67	1.02		
	6	Solid wire	264	26.9	+ 7.14	0.99		
	7	Solid wire	260	26.6	+ 7.14	0.97		
	8	Solid wire	260	26.6	− 6.67	1.04		
	9	Solid wire	255	26.6	+ 7.69	0.88		
	10	Solid wire	260	26.6	− 3.45	2.00		
	11	Solid wire	267	26.6	+ 5.88	1.21		
	12	Solid wire	263	26.7	− 5.88	1.19		
JT2-2-07	1	Flux cored	270	23.9	+ 6.67	0.97	63 + 68	0.58
	2	Flux cored	270	23.9	+ 8.33	0.77		
	3	Flux cored	270	23.9	+ 4.55	1.42		
	4	Flux cored	266	23.8	+ 5.26	1.20		
JT2-2-08	1	Flux cored	253	23.1	+ 6.25	0.94	90 + 86	0.72
	2	Flux cored	253	23.1	+ 7.14	0.82		
	3	Flux cored	245	22.8	+ 5.88	0.95		
	4	Flux cored	248	22.7	+ 6.25	0.90		
	5	Flux cored	245	22.8	+ 5.88	0.95		
	6	Flux cored	245	22.4	+ 4.76	1.15		
JT2-2-09	1	Flux cored	240	22.3	+ 5.88	0.91	133 + 136	0.32
	2	Flux cored	235	22.1	+ 6.67	0.78		
	3	Flux cored	242	22.2	+ 7.14	0.75		
	4	Flux cored	242	22.2	+ 7.14	0.75		
	5	Flux cored	242	22	+ 6.25	0.85		
	6	Flux cored	242	22	+ 6.25	0.85		
	7	Flux cored	242	22	+ 6.67	0.80		
	8	Flux cored	241	22.4	+ 5.88	0.92		
	9	Flux cored	231	22.5	+ 5.88	0.88		
	10	Flux cored	248	22.7	+ 6.25	0.90		
	11	Flux cored	240	22.7	+ 6.25	0.87		
	12	Flux cored	249	22.6	+ 5.88	0.96		

4 Numerical research program

A complex finite element model has been developed in ANSYS 17.2 [26] to simulate welding processes for civil engineering applications. Uncoupled transient thermomechanical analysis is performed, which is a comprehensive technique for welding simulations that is used for determining and evaluating temperature fields and residual stresses and deformations. The most important features of the method implemented in the code are presented hereunder.

Table 6 Welding variables, size of fusion zone, and maximum transverse deformation for single-bevel butt welds

Specimen	#	Filler metal	I (A)	U (V)	v (mm/s)	q (kJ/mm)	A_{FZ} (mm^2)	$U_{x,max}$ (mm)
JT3-1-01	1	Solid wire	280	28.1	+ 3.85	2.04	175	9.39
	2	Solid wire	280	28.1	+ 3.85	2.04		
	3	Solid wire	280	28.1	+ 3.85	2.04		
	4	Solid wire	270	27.8	+ 5.00	1.50		
JT3-1-02	1	Solid wire	280	28.1	+ 5.00	1.57	177	12.68
	2	Solid wire	281	28.2	+ 5.00	1.58		
	3	Solid wire	280	28.5	+ 2.94	2.71		
	4	Solid wire	270	27.2	+ 5.00	1.47		
JT3-1-03	1	Solid wire	280	28.2	+ 3.33	2.37	186	12.07
	2	Solid wire	280	28.5	+ 3.44	2.32		
	3	Solid wire	280	28.1	+ 5.00	1.57		
	4	Solid wire	270	27.2	+ 5.00	1.47		
JT3-2-01	1	Flux cored	260	23.1	+ 3.85	1.56	158	8.85
	2	Flux cored	238	23	+ 3.13	1.75		
	3	Flux cored	245	23	+ 5.00	1.13		
	4	Flux cored	242	23.1	+ 4.17	1.34		
	5	Flux cored	250	22.9	+ 5.00	1.15		
JT3-2-02	1	Flux cored	281	23	+ 3.85	1.68	158	9.99
	2	Flux cored	250	23.5	+ 3.57	1.65		
	3	Flux cored	260	23.2	+ 5.26	1.15		
	4	Flux cored	254	23.2	+ 4.55	1.30		
	5	Flux cored	270	23.2	+ 5.00	1.25		
JT3-2-03	1	Flux cored	281	23	+ 3.85	1.68	143	7.99
	2	Flux cored	280	23.2	+ 3.57	1.82		
	3	Flux cored	270	23.2	+ 3.33	1.88		
	4	Flux cored	270	23.2	+ 5.26	1.19		

Uncoupled thermomechanical analysis means that calculated temperature fields are applied as nodal loads in the subsequent mechanical analysis. The typical couplings in a thermo-metallurgical-mechanical analysis (Fig. 13) according to [1, 3, 27] are listed below; weak couplings and phase transformation-related phenomena are not taken into account in this paper:

1a Thermal expansion depends on microstructure of material.
1b Volume changes due to phase transformations.
1c Elastic and plastic material behaviors depend on microstructure.
1d Transformation-induced plasticity.
2a Microstructure evolution depends on deformation (weak coupling).
2b Phase transformations depend on stress state (weak coupling).
3a Thermal material properties depend on microstructure.
3b Latent heats due to phase transformations/solidification/melting.
4 Microstructure evolution depends on temperature.
5a Deformation evolution depends on temperature.
5b Mechanical material properties depend on temperature.
6a Deformation changes thermal boundary conditions (weak coupling).
6b Heat due to thermal, elastic and plastic strain rate (weak coupling).

In the current study, solid elements are used in the finite element model. A thermal solid element, SOLID70, with three-dimensional thermal conduction capability is applied

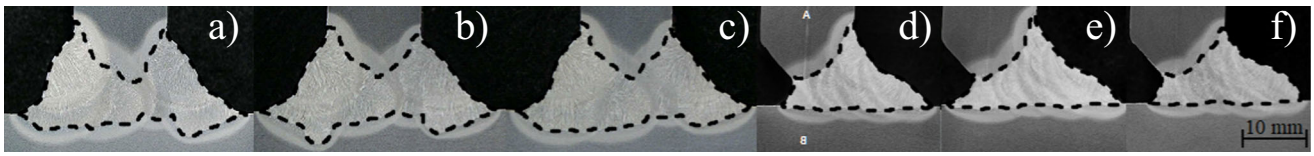

Fig. 5 Macrographs of double-bevel butt welds: **a**)–**c**) JT1-1-01–JT1-1-03 and **d**)–**f**) JT1-2-01–JT1-2-03

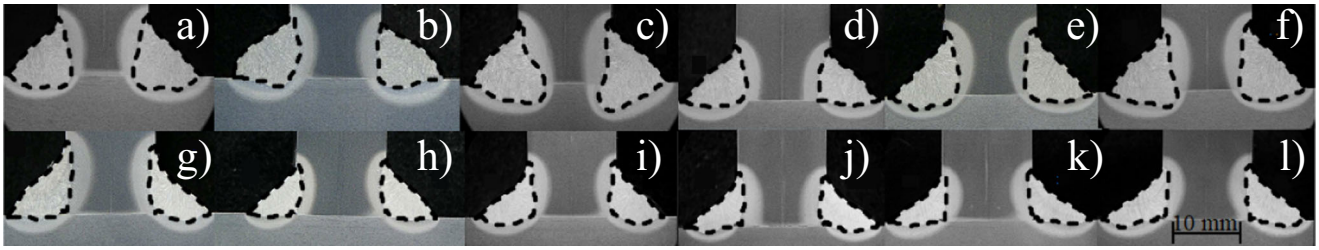

Fig. 6 Macrographs of double-sided fillet welds (single-pass welding): **a**)–**f**) JT2-1-01–JT2-1-06 and **g**)–**l**) JT2-2-01–JT2-2-06.

for modeling the heat transfer problem. The element has eight nodes with a single thermal degree of freedom at each node. It allows for prism, tetrahedral, and pyramid degenerations when used in irregular regions. An equivalent structural solid element, SOLID185, is used in the mechanical analysis which has eight nodes with three translational degrees of freedom (in nodal x, y, and z directions) at each node.

Thermal boundary conditions are defined for heat flow calculations. The initial temperature (room temperature or preheating temperature) of nodes is specified before the first load step of the thermo-metallurgical analysis. Nodal temperatures of not yet deposited weld passes are prescribed in the first step of the calculation to avoid ill-conditioned matrices. A combined temperature-dependent heat transfer coefficient $h_{cr}(T)$ is defined in the Function Editor of ANSYS [28] to model the effect of convection and radiation to ambient as described by Eq. (3). In the equation below

$$h_{cr}(T) = h_c(T) + \sigma\varepsilon(T)\left(T + T_{amb}\right)^2\left(T^2 + {T_{amb}}^2\right) \tag{3}$$

where $h_c(T)$ is convective heat transfer coefficient or film coefficient, T is absolute surface temperature, T_{amb} is absolute ambient temperature, σ is the Stefan-Boltzmann constant, and $\varepsilon(T)$ is emissivity. The film coefficient is assumed to be 25 W m^{-2} K^{-1}, while emissivity is taken as a temperature-independent value with a magnitude of 0.8 in the current research. On the other hand, moving volumetric heat sources induce heat generation which is defined as element body force load during the transient thermo-metallurgical analysis. The double ellipsoidal heat source model is implemented in the current study. Equations (4) and (5) determine the power density distribution in the front and rear quadrants, respectively

$$q_f(x,y,z) = q_{max} \cdot e^{-3\frac{x^2}{{c_f}^2} - 3\frac{y^2}{a^2} - 3\frac{z^2}{b^2}} \tag{4}$$

$$q_r(x,y,z) = q_{max} \cdot e^{-3\frac{x^2}{{c_r}^2} - 3\frac{y^2}{a^2} - 3\frac{z^2}{b^2}} \tag{5}$$

where characteristic parameters c_f, c_r, b, and a represent the physical dimensions of the heat source model in each direction as shown in Fig. 14, while the maximum power densityq_{max} is used for numerical scaling of power density; thus, the law of conservation of energy is fulfilled and heat generation error due to mesh formulation can be eliminated in the transient analysis at each time step. The size of front and rear ellipsoids could be calibrated and fitted separately, while it could be applied even to simulate deep penetration welding. Several analogous functions exist to describe the power density distribution of a double ellipsoidal heat source, e.g., Bradac [29] used different constants in the exponent for each direction instead of a value of 3. Due to lack of sufficient data, Goldak, Chakravarti, and Bibby [21] assumed that it is reasonable to take the distance in front of the source equal to one half of the weld width ($c_f = a$) and the distance behind the source equal to twice the weld width ($c_r = 4a$) as a first approximation. The idea of using a double ellipsoidal heat source model instead of a single ellipsoidal one is explained by Goldak [30] as an attempt to generate typical weld pool shapes capturing the "digging action of the arc" in front and "slower cooling of the weld by conduction of heat into the base metal" at the rear. In general, it is recommended by Goldak et al. [31] that the heat source may not move more than half of the weld pool length to function appropriately in three-dimensional welding simulations using the transient method.

In the mechanical analysis, temperature fields are applied as nodal loads as explained before. Clamping conditions (i.e., rotational and translational degree of freedom constraints) have an important impact on the evolution of deformations and stresses. Even the release time of clamps has an

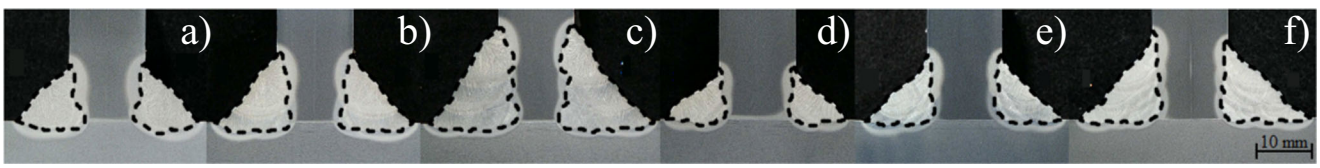

Fig. 7 Macrographs of double-sided fillet welds (multi-pass welding): **a**)–**c**) JT2-1-07–JT2-1-09 and **d**)–**f**) JT2-2-07–JT2-2-09

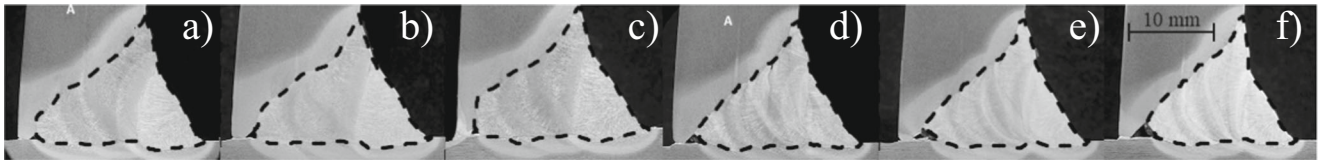

Fig. 8 Macrographs of single-bevel butt welds: **a**)–**c**) JT3-1-01–JT3-1-03 and **d**)–**f**) JT3-2-01–JT3-2-03

appreciable influence on residual stresses and deformations. First of all, rigid body motion has to be avoided. Therefore, defining the minimum number of constraints is necessary to analyze a statically determinate structure. In addition, clamps can fundamentally act like rigid (or elastic) supports. In the case of statically indeterminate structures, the additional constraints have to be deleted in an intermediate (hot release) or in the last sub-step (cold release) of the simulation to assess residual stresses and deformations.

Depending on the welding process, welded joints can be created with or without filler material addition. Therefore, initial gaps and deposited material have to be modeled in the welding simulation. The "birth and death' procedure [27] is added in the thermal analysis in the numerical simulation. Element activation and deactivation can be executed using the EALIVE and EKILL commands, respectively. EKILL uses a stiffness matrix multiplier of 10^{-6} (it can be changed via ESTIF command) by default for deactivated elements. In the mechanical analysis, the quiet element technique [32] is implemented instead of "birth and death" procedure presented previously, since all elements are active from the beginning of the calculation. According to [33, 34], extremely reduced Young's modulus can cause numerical problems; therefore, a reduction of two orders of magnitude is sufficient. Therefore, Young's modulus of 1000 MPa is used for un-deposited material, while linear thermal expansion coefficient is temperature-independent and taken as zero to ensure thermal strain free bead elements before welding. Material model changes for weld bead elements only above 1200 °C as it is considered to be the reference temperature.

In the current investigation, material properties are based on EN 1993-1-2:2005 [35], which is basically recommended for structural fire design, but there are several examples (e.g., [6–8, 36, 37]) demonstrating its applicability for welding simulation purposes as well. The material properties are defined between 20 and 1200 °C in the standard. Temperatures can be much higher during welding; therefore, material properties are set as constant values above 1200 °C. Temperature-dependent thermal material properties, such as thermal conductivity, specific heat, and density, are defined in the standard. However, enthalpy is considered in the simulation instead of density and specific heat; therefore, peaks, because of latent heats due to 훼-phase to γ-phase transformation (and vice versa) and solidification/melting, in specific heat can be handled in the numerical model in a more convenient manner (Fig. 15). Eurocode uses reduction factors for considering temperature-dependent Young's modulus ($k_{E,\theta}$), yield strength ($k_{y,\theta}$), proportional limit ($k_{p,\theta}$), and stress-strain curves (Fig. 16). This material model has a notable advantage: only yield strength (355 MPa in the current paper) and Young's modulus are needed to be known on room temperature to describe the mechanical behavior of the material. The required parameters are given in the Annex A of EN 1993-1-2 to describe stress-strain curves. It also gives a recommendation for modeling hardening below 400 °C. A multilinear isotropic hardening model is used in the simulations assuming the von Mises yield criterion. Large deflection effects are also taken into account in the mechanical analysis.

5 Numerical results

5.1 Sensitivity analysis

The sensitivity analysis focuses on the effect of thermal efficiency and characteristic parameters of the heat source

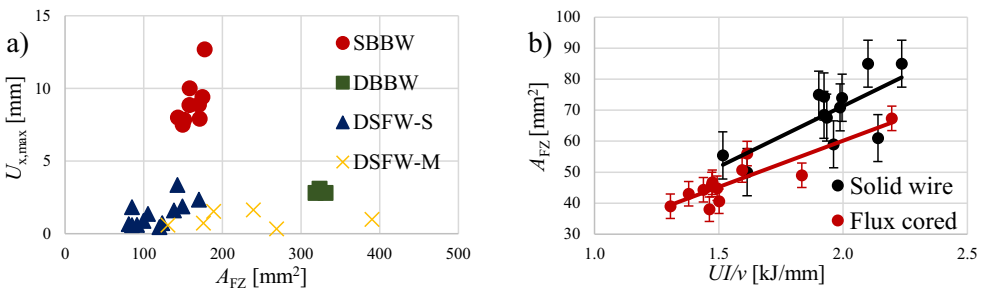

Fig. 9 Fusion zone size vs. **a**) maximum transverse deformations and **b**) total heat input per unit length

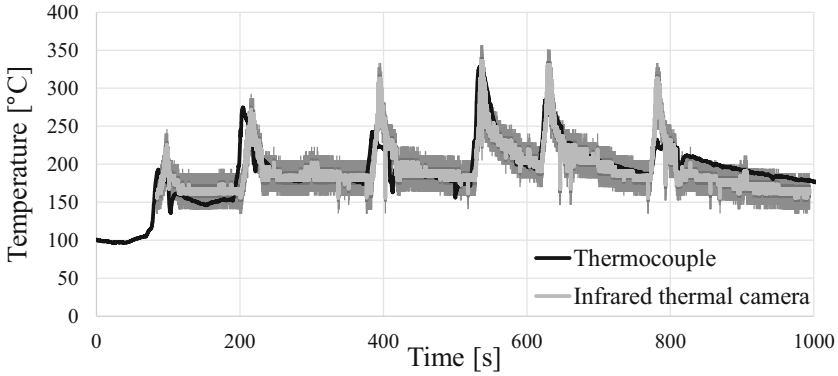

Fig. 10 Temperature measurements of a thermocouple and the calibrated infrared thermal camera

model. Solely solid wire electrodes are assumed in the calculations as the only aim of the sensitivity analysis is to evaluate the magnitude of differences in weld pool sizes, transverse deformations, and von Mises residual stresses. The dimensions of T-joints with double-sided fillet weld are identical to the experimental ones, while throat thickness is 5 mm. A gap of 0.5 mm filled with "un-deposited material" is modeled between the base plate and the stiffener. The model consists of 27,010 finite elements (Fig. 17). The minimum number of constraints is defined to analyze a statically determinate structure. Interpass temperature is not controlled, the second weld pass is laid right after the first weld pass with the same welding direction. Welding variables are $I = 270$ A, U is calculated using Eq. (1), assuming solid wire electrodes, and $v = 4$ mm s^{-1}. Assuming flux cored electrodes in the calculation of voltage would only affect the heat input, while using different thermal efficiencies has the same effect. Ambient temperature is taken as 20 °C, while preheat temperature is 150 °C. The reference values for the characteristic parameters of Goldak's double ellipsoidal heat source model are $a = b = c_f = 2.5$ mm and $c_r = 4c_f$. These parameters are scaled in the sensitivity analysis to investigate the effect of power density distribution. Scaling factors of 1.00, 1.50, 2.00, 2.50, and 3.00 are applied; thermal efficiency is set to 1.00. Five additional analyses are performed in order to analyze the influence of thermal efficiency, which is increased in 0.10 steps from 0.60 to 1.00, while heat source parameters are set to the reference values. Figures 18, 19, and 20 present the results of the sensitivity analysis.

Figure 18 shows weld pool size and isothermal lines in the vicinity of the weld in the midsection during welding of the first weld bead. Arrows show increasing tendency of fusion zone size. Scaling the reference heat source parameters results in lower power density. Thus, weld pool size decreases as scaling factor increases. Temperature does not even reach the liquidus temperature, assumed to be 1500 °C, in the weld bead elements when the scaling factor is equal to 3.00. The cross-sectional area of the weld pool is 47.5 mm^2, 45.5 mm^2, 36 mm^2, 12.5 mm^2, and 0 mm^2 using scaling factors of 1.00, 1.50, 2.00, 2.50, and 3.00, respectively. Variation of thermal efficiency has a similar effect as it has an influence on power density distribution; weld pool size increases as thermal efficiency increases. The cross-sectional area of the weld pool is 25 mm^2, 32 mm^2, 37 mm^2, 42.5 mm^2, and 47.5 mm^2 using thermal efficiency of 0.60, 0.70, 0.80, 0.90, and 1.00, respectively.

Figure 19 sums up the transverse deformations of the joint after cooling. Configurations a)–e) have maximum transverse deformations of 1.56 mm, 1.46 mm, 1.26 mm, 0.93 mm, and 0.45 mm, respectively. Transverse deformation of the stiffener decreases as scaling factor increases. Arrows show increasing tendency of deformations. For instance, scaling factor of 2.00 results in a 20% decrease in deformations in comparison to the reference

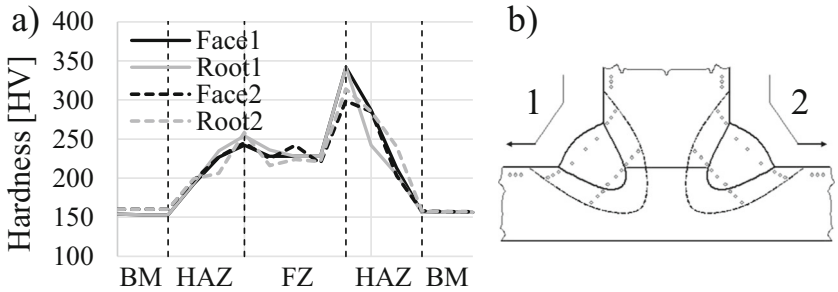

Fig. 11 **a**) Hardness profile for JT2-1-01 and **b**) points for measurements

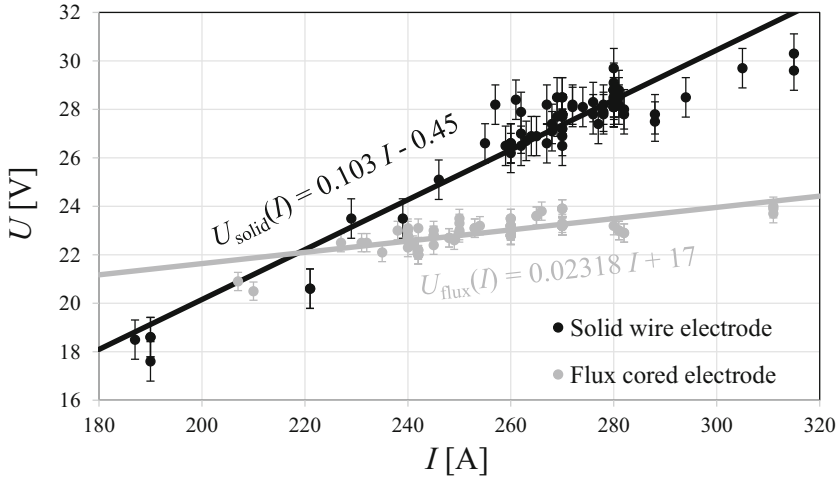

Fig. 12 Operating points and the relationship between current and voltage for solid wire and flux cored electrodes

configuration. Obviously, configurations d) and e) are erroneous as temperature just reaches the reference temperatures in the finite elements representing the weld bead (Fig. 18), while the elevated temperature is lower than liquidus temperature in the corresponding finite elements. Configurations f)–j) have maximum transverse deformations of 1.41 mm, 1.46 mm, 1.54 mm, 1.58 mm, and 1.56 mm, respectively. Transverse deformation of the stiffener slightly increases as thermal efficiency increases; however, the variation is within 10% due to 67% increase in thermal efficiency.

Figure 20 shows the von Mises residual stresses in the vicinity of the weld beads in midsection after cooling. The plastic zones are shown in the figure, where the residual stress is higher than the yield strength, which is 355 MPa in this case. The same conclusions can be drawn as for Fig. 19. Arrows show increasing tendency of plastic zone size. Plastic zone size decreases as the weld pool size decreases. The signs of lack of fusion are presented for configuration e) for instance, where several finite elements in the weld bead remain elastic, while quasi-zero penetration is simulated in the joint.

Results show that thermal efficiency and the scaling factor may have a similar effect on residual stresses and transverse deformations. However, it is important to emphasize that sufficient power density is required to reach the reference temperature of un-deposited material; otherwise, the material model for weld bead elements remains elastic with a low Young's modulus. It results in quasi-zero stresses in weld beads due to lack of fusion affecting overall residual stresses in conjunction with obtaining equilibrium of resultant internal forces and bending moments in any section of the specimen. On the other hand, 100% increase in scaling factor for the first three cases results in a variation of 32% in the weld pool size, while the variation is within 90% due to 67% increase in thermal efficiency.

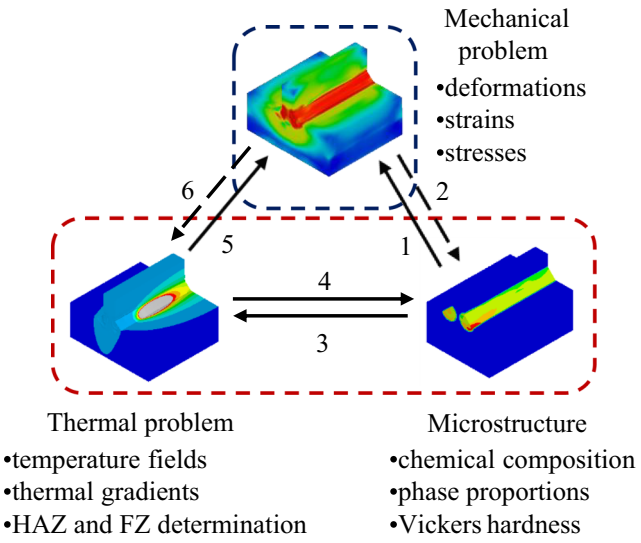

Fig. 13 Couplings in a thermo-metallurgical-mechanical analysis

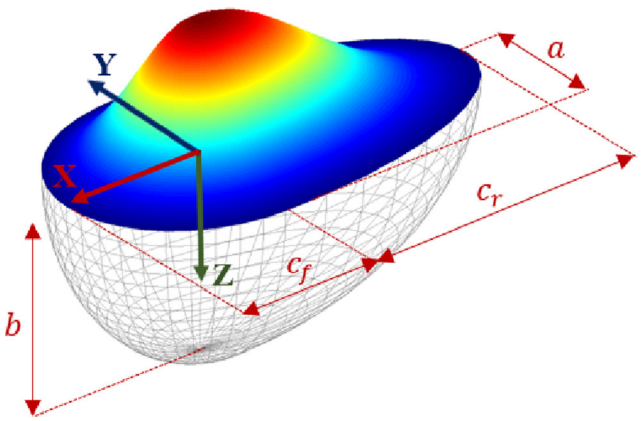

Fig. 14 Notations and power density distribution of the double ellipsoidal heat source model

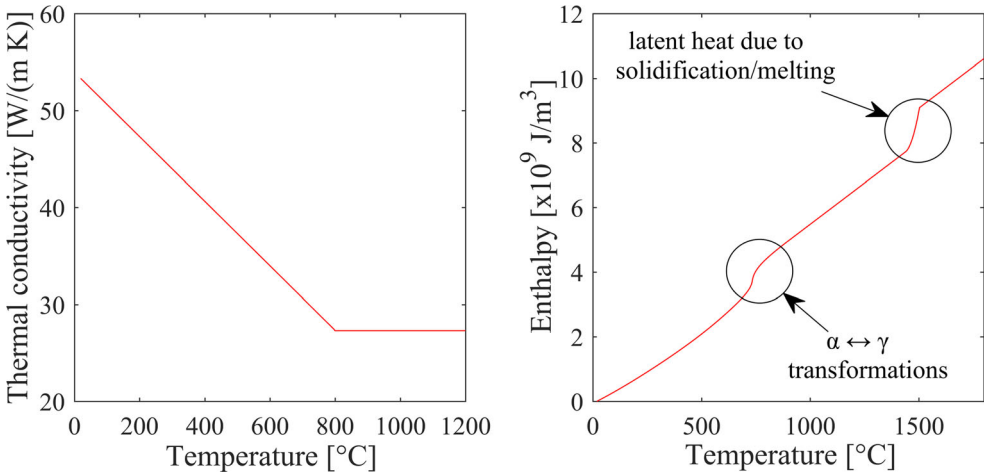

Fig. 15 Thermal material properties based on EN 1993-1-2:2005 [35]

5.2 Evaluation of thermal efficiency

Generally, thermal efficiency of a welding process can be evaluated using several approaches. In the current study, it is determined by the comparison of experimental and numerical data. Thermocouples and infrared thermal imaging are utilized to carry out temperature measurements during welding, as presented in Section 3; thus, thermal cycles determined by finite element models can be compared with experimental data. In addition, macrographs are used to evaluate the thermal efficiency as well. Nevertheless, EN 1011-1:2009 [38] recommends to use 0.80 as thermal efficiency, while Radaj [27] introduced a range between 0.65 and 0.90 for metal active gas welding. The sensitivity analysis in the previous section shows that thermal efficiency has a larger effect on fusion zone size than scaling the characteristic parameters of the heat source, while the latter has a negligible effect on total (elastic and thermal) strains and temperatures further from the weld bead as presented by Kollár and Kövesdi [8].

T-joints with double-sided fillet weld (JT2-1-06 and JT2-2-02 welded with solid wire and flux cored electrodes, respectively) are chosen for the determination of thermal efficiency. The actual dimensions of the joints are modeled with the corresponding throat thicknesses. Throat thicknesses are

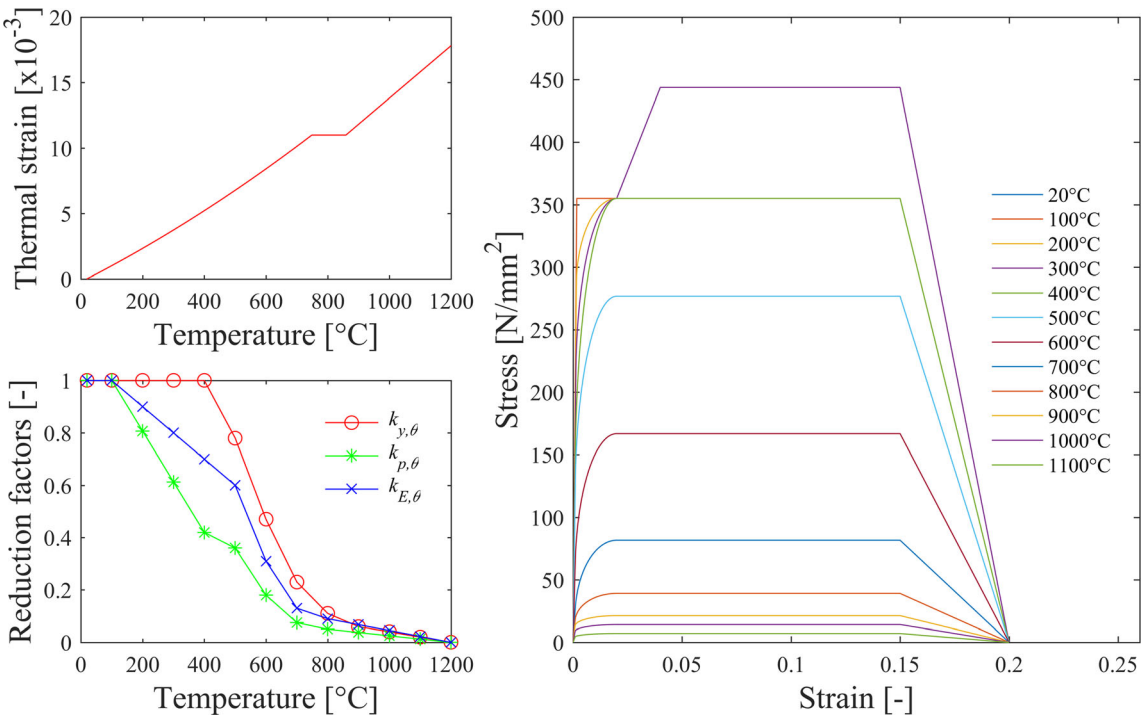

Fig. 16 Mechanical material properties based on EN 1993-1-2:2005 [35]

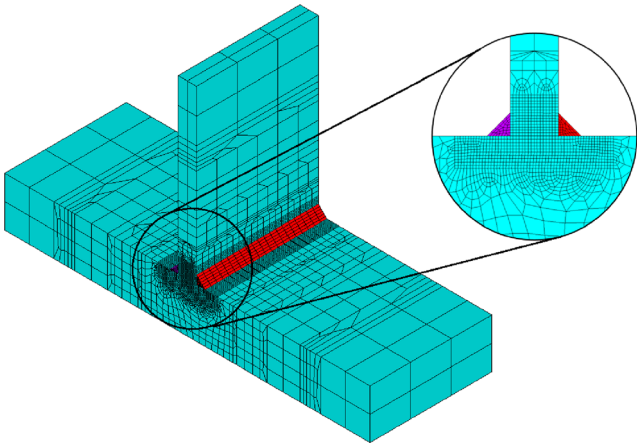

Fig. 17 Finite element model of a T-joint with double-sided fillet weld

measured on the macrographs for the weld beads which are single-pass welded; models are built up with average throat thicknesses. The second weld pass is laid after the first weld pass with opposite welding direction. Welding variables are identical to the values registered during the tests and are summed up in Table 4. Ambient temperature is 20 °C, while preheat and interpass temperatures are both taken as 150 °C. The characteristic parameters of Goldak's double ellipsoidal heat source model are $a = b = 10$ mm and $c_r = c_f = 2.5$ mm for both specimens. Nodes in the stiffener in the midsection, 10 mm above the base plate, are chosen for the comparison of experimental and numerical data as presented in Fig. 21. The figure shows the time-temperature curves based on infrared thermal imaging ("Measurement") and the finite element analysis ("FEA"). The peak temperature is approximately 700–800 °C for both cases and the cooling phenomenon is also simulated successively. The temperature is about 200 °C at 200 s in the case of the investigated configurations for both approaches. The figure presents the macrograph of the JT2-1-06 specimen as well and a cross section of the finite element model denoting the fusion zone (and the heat-affected zone in the case of the macrograph). The calibration is based on the fusion zone size. The aim is to approximate the measured fusion zone size within an arbitrary ± 10% range specified for handling uncertainties in welding variables. The cross-sectional areas of the fusion zones for JT2-1-06, by measurements, are 75 mm^2 and 74 mm^2 for the first and second weld beads, respectively. In addition, fusion sizes are 43 mm^2 and 39 mm^2 for JT2-2-02. The corresponding simulated weld pool sizes are 68 mm^2, 67 mm^2, 42 mm^2, and 37 mm^2, respectively, which are within the reasonable range. According to the results of the sensitivity analysis, the influence of thermal efficiency is already known in the case of the actual T-joint; therefore, thermal efficiency is changed in 0.10 steps. Thermal efficiency (η) of 0.90 is accepted related to the comparison of numerical and experimental data and it is applied in the simulations hereafter for both electrodes.

5.3 Calibration and verification of the double ellipsoidal heat source model

In this section, the characteristic parameters of the implemented double ellipsoidal heat source model are calibrated for a typical range of welding variables in the case of double-sided fillet welds with single weld passes. The developed weld process model for welding simulation of double-sided fillet welds

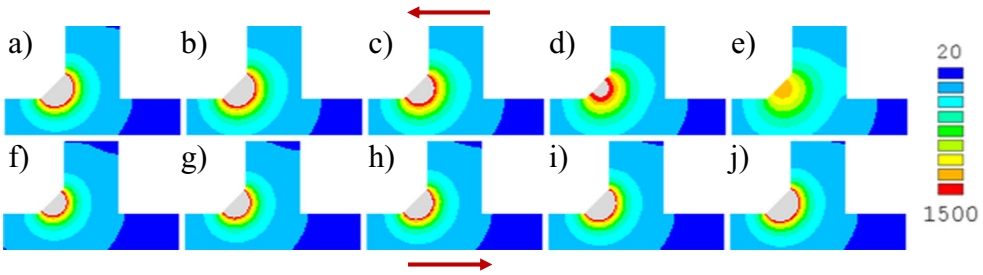

Fig. 18 Size of the fusion zone in (mm^2) using heat source parameter scaling factors of **a**) 1.00, **b**) 1.50, **c**) 2.00, **d**) 2.50, and **e**) 3.00 and thermal efficiency of **f**) 0.60, **g**) 0.70, **h**) 0.80, **i**) 0.90, and **j**) 1.00

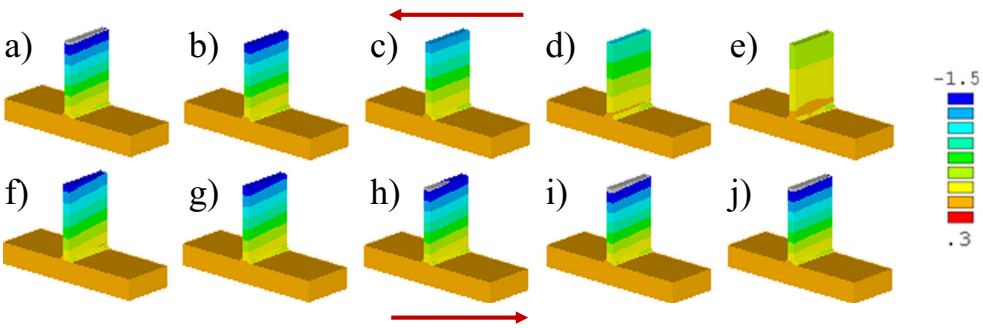

Fig. 19 Transverse deformations in (mm) using heat source parameter scaling by **a**) 1.00, **b**) 1.50, **c**) 2.00, **d**) 2.50, and **e**) 3.00 and thermal efficiency of **f**) 0.60, **g**) 0.70, **h**) 0.80, **i**) 0.90, and **j**) 1.00

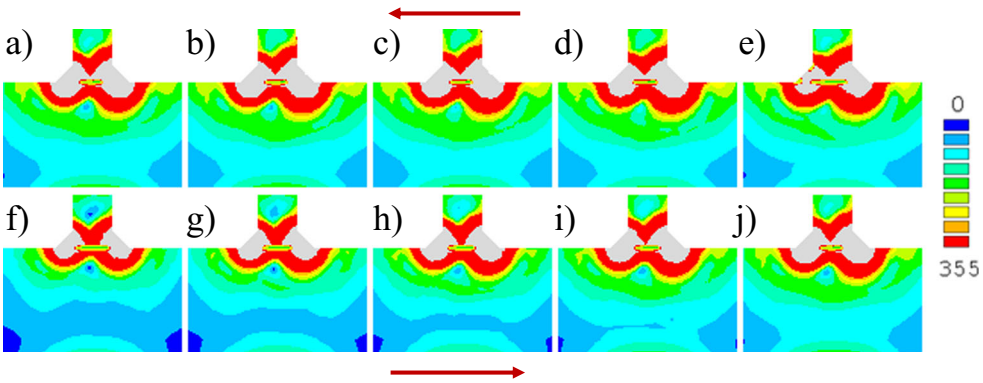

Fig. 20 von Mises residual stresses in (MPa) using heat source parameter scaling by **a**) 1.00, **b**) 1.50, **c**) 2.00, **d**) 2.50, and **e**) 3.00 and thermal efficiency of **f**) 0.60, **g**) 0.70, **h**) 0.80, **i**) 0.90, and **j**) 1.00

with single weld passes is verified. A total of 12 specimens are modeled in the numerical research program.

Double-sided fillet welded T-joints with single-pass welds are investigated. The actual dimensions of the joints are modeled with the corresponding throat thicknesses. The parametric model of Section 5.2 is used in the simulations applying welding variables according to Table 7. The table sums up welding variables, net heat input per unit length $q_{net} = \eta UI/v$, Goldak's heat source parameter a, fusion zone sizes A_{FZ}, and $A_{FZ,FEA}$ based on measurements and numerical analyses and error in simulated fusion zone size, respectively. Voltage is calculated using Eqs. (1) and (2) depending on the type of filler metal. After performing dozens of iterations, a function of heat input per unit length is developed to evaluate a and b characteristic parameters of Goldak's double ellipsoidal heat source model. The characteristic parameters a and b for specimen JT2-2-02 are outliers (italic letters) in data; therefore, the specimen is ignored when the $a(q_{net})$ polynomial function is approximated. The $A_{FZ,FEA}$ fusion zone sizes in the table are determined by characteristic parameters using Eq. (6),

$$a(q_{net}) = 11.094{q_{net}}^3 - 62.383{q_{net}}^2 + 117.52q_{net} - 60.812\ (\text{mm});\ c_r = c_f = 2.5\ \text{mm} \quad (6)$$

for flux cored electrodes. The model for this configuration assumes that $a = b$ and $c_r = c_f = 2.5$ mm regarding previous simulations of the joints. The characteristic parameters of Goldak's double ellipsoidal heat source model are independent of the net heat input per unit length q_{net} for the configurations welded with solid wire electrode ($a = b = 10$ mm and $c_r = c_f = 2.5$ mm). Obviously, the small c_r and c_f parameters result in a requirement of dense mesh along welding trajectory. Minimum and maximum errors are − 9.9% and 9.8%, while the mean and standard deviation of errors are − 1.9% and 6.0%, respectively.

Figure 22 shows a nomogram for the developed approach. Selecting welding current, this may be wire feed rate for MIG/MAG welding power sources, determines voltage for solid wire or flux cored electrodes. Typical travel speeds and corresponding net heat inputs per unit length are shown as well for the two types of filler metals. Finally, characteristic parameters are evaluated using the curves of the figure or Eq. (6). The $U(I)$, $a(q_{net})$, and $b(q_{net})$ equations are implemented in the finite element code for further parametric studies and the sustainable virtual manufacturing of stator segments of a wind turbine as a final application in the future.

5.4 Validation of the weld process model

Calibration and verification of the heat source model make it possible to investigate the effect of additional parameters and variants in qualitative and quantitative parametric studies and virtual prototyping. It is a time-consuming method, while there is a large amount of waste during the

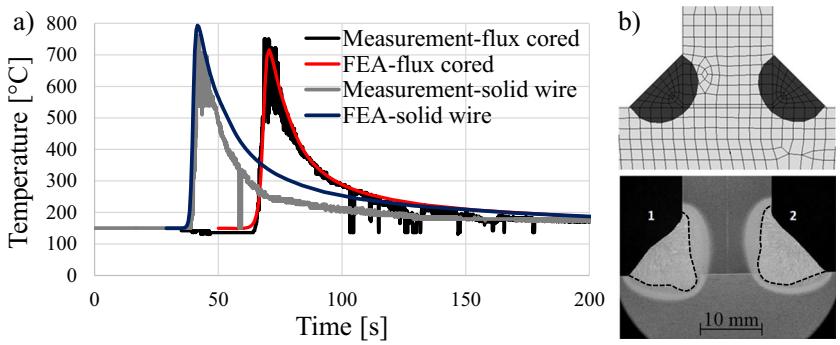

Fig. 21 Determination of thermal efficiency by **a**) temperature measurements for flux cored and solid wire electrodes and **b**) a macrograph of specimen JT2-1-06

Table 7 Input and output data for the calibrated cases

Specimen	#	Filler metal	I (A)	U (V)	v (mm/s)	q_{net} (kJ/mm)	a (mm)	A_{FZ} (mm^2)	$A_{FZ,FEA}$ (mm^2)	Error (%)
JT2-1-01	1	Solid wire	270	27.4	4.00	1.66	10	69	67	− 2.2
	2	Solid wire	270	27.4	− 4.00	1.66	10	74	67	− 9.9
JT2-1-02	1	Solid wire	221	22.3	2.13	2.08	10	61	67	9.8
	2	Solid wire	221	22.3	− 2.32	1.91	10	59	64	8.5
JT2-1-03	1	Solid wire	315	32.0	4.17	2.18	10	85	87	2.4
	2	Solid wire	315	32.0	− 4.55	1.99	10	85	83	− 2.4
JT2-1-04	1	Solid wire	239	24.2	3.70	1.40	10	55	51	− 7.9
	2	Solid wire	229	23.1	− 3.33	1.43	10	50	49	− 2.0
JT2-1-05	1	Solid wire	280	28.4	4.00	1.79	10	71	73	3.0
	2	Solid wire	261	26.4	− 3.85	1.61	10	68	65	− 3.8
JT2-1-06	1	Solid wire	305	31.0	4.77	1.78	10	75	68	− 9.3
	2	Solid wire	280	28.4	− 4.17	1.72	10	74	67	− 9.5
JT2-2-01	1	Flux cored	282	23.5	2.92	2.05	13.5	67	68	1.5
	2	Flux cored	282	23.5	− 4.00	1.49	12.5	56	51	− 8.9
JT2-2-02	*1*	*Flux cored*	*210*	*21.9*	*2.94*	*1.41*	*10.0*	*43*	*40*	*− 7.0*
	2	*Flux cored*	*210*	*21.9*	*− 3.33*	*1.24*	*10.0*	*39*	*35*	*− 10.3*
JT2-2-03	1	Flux cored	311	24.2	5.00	1.36	11.5	45	48	6.7
	2	Flux cored	311	24.2	− 5.00	1.36	11.5	47	49	4.3
JT2-2-04	1	Flux cored	265	23.1	4.17	1.32	11.2	41	42	2.4
	2	Flux cored	265	23.1	− 4.35	1.27	10.5	44	43	− 2.3
JT2-1-05	1	Flux cored	232	22.4	3.57	1.31	11.0	38	39	2.6
	2	Flux cored	232	22.4	− 3.70	1.26	10.5	43	41	− 4.7
JT2-1-06	1	Flux cored	311	24.2	4.55	1.49	12.5	51	51	0.0
	2	Flux cored	270	23.3	− 4.17	1.36	11.5	49	46	− 6.1

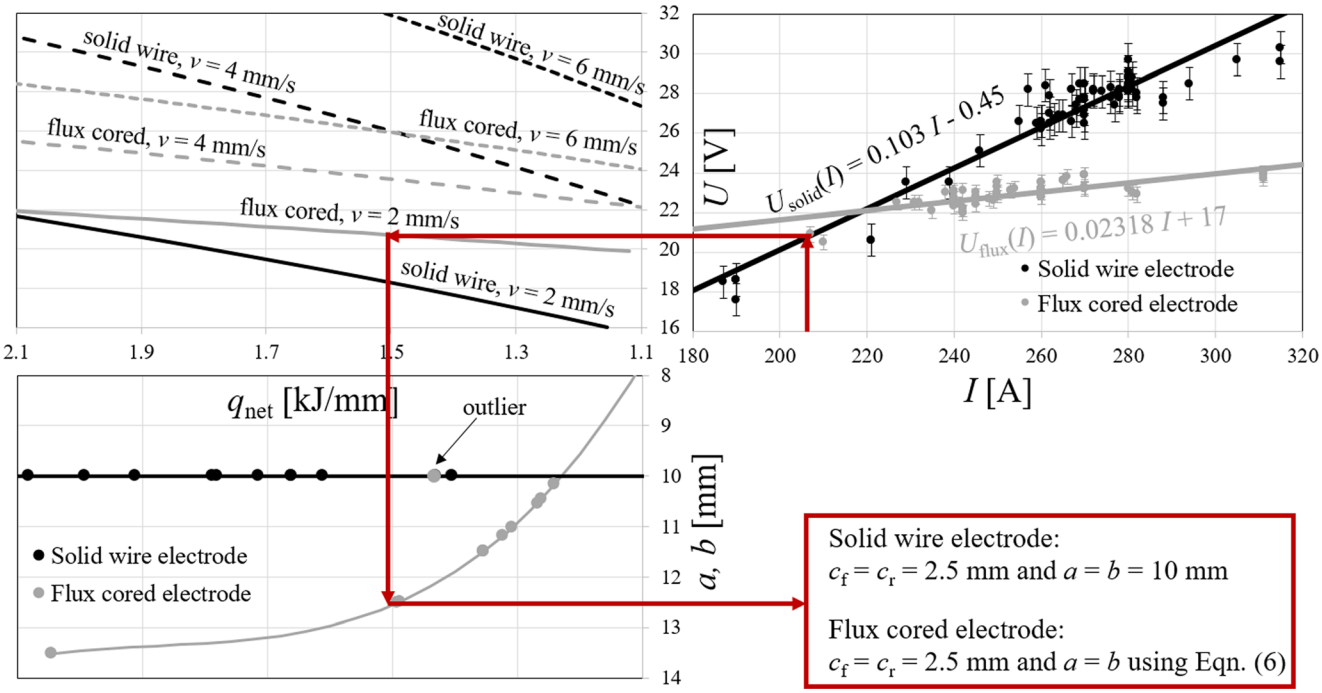

Fig. 22 Workflow of determining characteristic parameters for virtual manufacturing

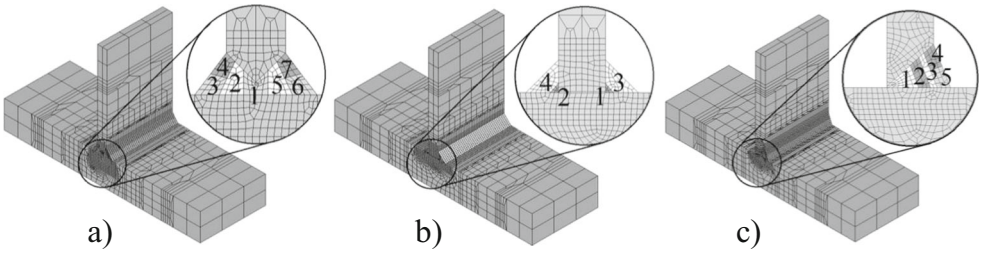

Fig. 23 Finite element models of **a**) JT1-1-03, **b**) JT2-1-07, and **c**) JT3-2-01

Table 8 Input and output data for the validated cases

Specimen	#	Filler metal	I (A)	U (V)	v (mm/s)	q_{net} (kJ/mm)	a (mm)	A_{FZ} (mm^2)	$A_{FZ,FEA}$ (mm^2)	Error (%)
JT1-1-03	1	Solid wire	190	19.12	+ 3.57	0.92	10	331 (298)	302	− 8.8 (1.3)
	2	Solid wire	280	28.39	+ 4.55	1.57	10			
	3	Solid wire	280	28.39	+ 5.26	1.36	10			
	4	Solid wire	270	27.36	+ 5.26	1.26	10			
	5	Solid wire	280	28.39	− 3.33	2.15	10			
	6	Solid wire	280	28.39	− 4.17	1.72	10			
	7	Solid wire	270	27.36	− 5.56	1.20	10			
JT2-1-07	1	Solid wire	278	28.18	+ 8.33	0.85	10	94 + 95	86 + 100	− 1.3
	2	Solid wire	262	26.54	+ 7.69	0.81	10			
	3	Solid wire	276	27.98	− 3.85	1.81	10			
	4	Solid wire	278	28.18	− 3.45	2.04	10			
JT3-2-01	1	Flux cored	260	23.03	+ 3.85	1.40	11.9	158	163	3.2
	2	Flux cored	238	22.52	+ 3.13	1.54	12.7			
	3	Flux cored	245	22.68	+ 5.00	1.00	5.4			
	4	Flux cored	242	22.61	+ 4.17	1.18	9.2			
	5	Flux cored	250	22.61	+ 5.00	1.03	6.1			

"trial and error" approach in the product development phase. Developing a sustainable virtual manufacturing process is an innovative way to reduce waste in workshops and specify optimal conditions depending on the requirements for advanced applications.

The verified parameters for double-sided fillet welds with single weld passes are validated using an extended set of parameters in the case of the three types of T-joint; one from each configuration is presented in this paper. Figure 23 shows the finite element models of the weldments contributing in the validation process. T-joints with double-bevel butt weld (JT1-1-03), with double-sided fillet welds using multiple passes (JT2-1-07), and with single-bevel butt weld (JT3-2-01) are studied. Models consist of

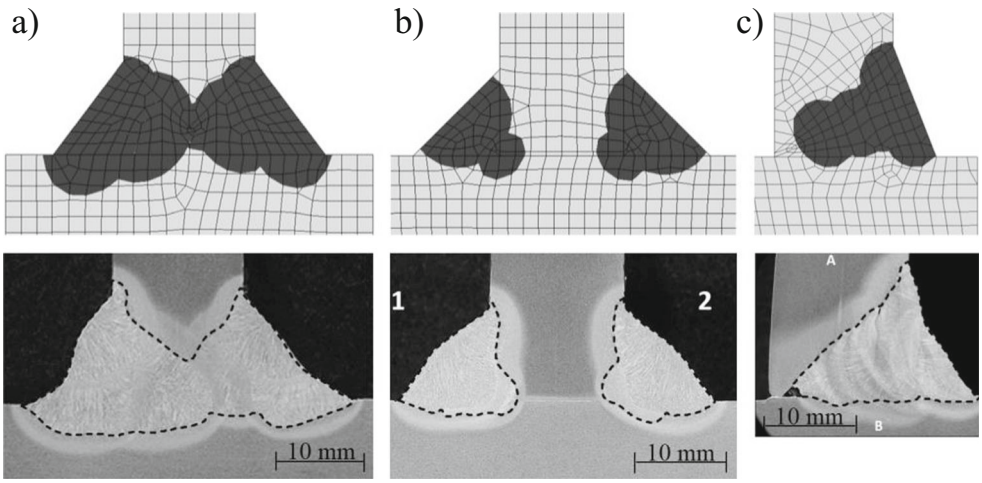

Fig. 24 Simulated and measured fusion zones for **a**) JT1-1-03, **b**) JT2-1-07, and **c**) JT3-2-01

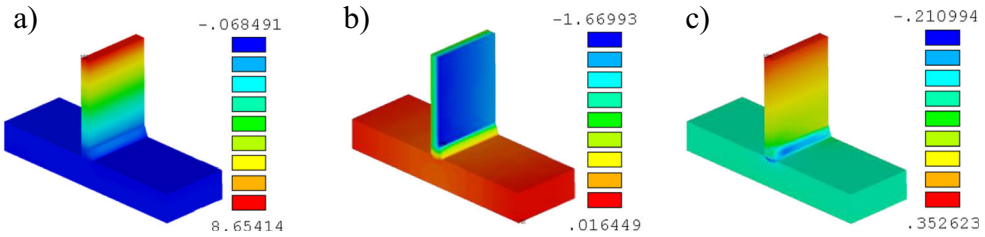

Fig. 25 Deformations in (mm) after cooling for JT3-2-01 in **a**) *x*, **b**) *y*, and **c**) *z* directions

26,052, 23,112 and 18,632 finite elements, respectively. Welding sequences are also summed up in Fig. 23 for the investigated cases. Table 8 sums up specimen notations and input and output data. Fusion zone sizes in the table are related to the whole joints as multi-pass welding is used for the weldments.

Figure 24 shows the simulated fusion zones and the macrographs highlighting fusion lines with dashed lines; liquidus temperature is assumed to be 1500 °C. Measurements and numerical results are in a good agreement for the specimens and the absolute maximum error in the cross-sectional area of the fusion zone is 8.8%, which is a quite convincing result. The calibrated and verified double ellipsoidal heat source model is validated for multi-pass welding using an extended set of parameters. The largest discrepancy comes forward in the case of JT1-1-03, which is T-joint with a double-bevel butt weld. However, the complex geometry of weld face is not taken into account in the simulations. Neglecting the difference between the perfect and imperfect weld face geometry reduces the difference to 1.3% as the measured fusion zone size becomes 298 mm^2. On the other hand, geometry of weld face does not have a large influence on results for the other T-joints.

Figure 25 presents deformations of the joints after cooling in *x*, *y*, and z directions for JT3-2-01. All the components are shown in the figure; however, transverse deformations are dominant in this case. Specimens a)–c) in Fig. 23 have maximum simulated transverse deformations of 2.19 mm (measurement 2.80 mm), 1.02 mm (measurement 1.53 mm), and 8.65 mm (measurement 8.85 mm), respectively. Results show that the double-bevel butt weld and the double-sided fillet weld have performed well in a distortion-controlled design. Obviously, the T-joint with single-bevel butt weld is the worst configuration in this sense. On the other hand, it is important to highlight that throat thickness varies for the three specimens.

The top nodes, representing the maximum transverse deformations, are selected and typical displacement data as a function of time are also given in Fig. 26 to show the importance of different joint configurations. The time limit in the figure is maximized in 1500 s for clarity; however, cooling to room temperature is modeled. Temperature is 150 °C in the first load step due to the preheat temperature. Welding time varies in a function of travel speed and number of weld passes for the validated cases. Transverse nodal displacement decreases after the fourth weld pass for JT1-1-03 and it is alternating for JT2-1-07 because of the welding sequence shown in Fig. 23. Obviously, transverse nodal displacement increases permanently during welding for the JT3-2-01 specimen which is a T-joint with a single-bevel butt weld. Eventually, the phenomenon shown in the figure is an unambiguous explanation for the beneficial effect of alternating welding sequence in a distortion-controlled design. Welding on alternating sides of the stiffener may result in quasi-zero deformations, such as in the case of JT2-1-07, while completing all the weld passes on one side of the stiffener after the other, such as in the case of JT1-1-03, may induce a worse case regarding residual deformations. However, it is important that throat thickness varies for the specimens.

A three-dimensional heat transfer model is used to predict the weld pool size in fillet and butt weld configurations during metal active gas welding. Eventually, the developed model is applicable to simulate the fusion zone size with fair precision in S355 structural steel weldments using M21 - ArC - 18

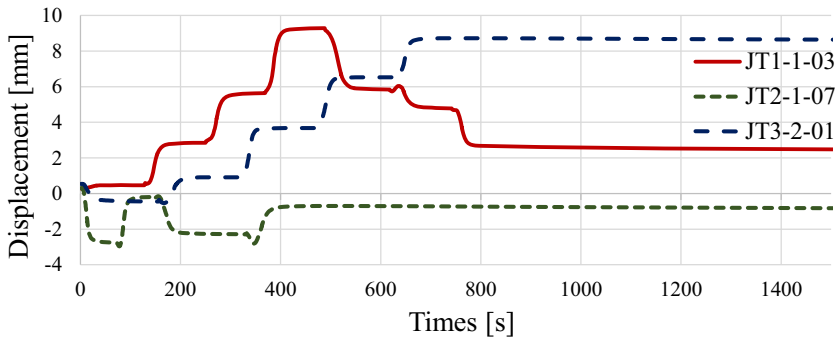

Fig. 26 Transverse displacement data as a function of time for the validated models

(Corgon 18) shielding gas, PA flat or PB horizontal-vertical welding positions, and two different electrode types.

6 Conclusions

Welding simulation has become an ultimate tool for virtual manufacturing, testing, and prototyping in the recent years; nevertheless, the calibration of heat source models used in finite element analysis is a common problem as the variation of welding variables has a large influence on the weld pool shape and size. The aim of the current research program is to develop a weld process model for a typical T-joint of a weldment. An experimental and numerical study is performed focusing on the size of fusion zone, deformations, and residual stresses during metal active gas welding investigating several types of T-joints and two different filler metals. The relationship between welding current and voltage for solid wire and flux cored electrodes, with diameters of 1.2 mm using a mixture of pure argon and carbon dioxide as shielding gas, is determined. A sensitivity analysis is performed focusing on the effect of thermal efficiency and characteristic parameters of the double ellipsoidal heat source model using uncoupled thermomechanical analysis. Results show that thermal efficiency and the scaling factor may have a similar effect on residual stresses and transverse deformations. However, it is important to emphasize that sufficient power density is requisite to reach the reference temperature of un-deposited material; otherwise, the material model for weld bead elements remains elastic with a low Young's modulus. It results in quasi-zero stresses in weld beads due to lack of fusion affecting overall residual stresses in conjunction with obtaining equilibrium of resultant internal forces and bending moments in any section of the specimen. The thermal efficiency of the welding process is determined by the comparison of experimental and numerical data. The heat source parameters of the implemented double ellipsoidal heat source model are calibrated for a typical range of welding variables in the case of double-sided fillet welds with single weld passes. The developed weld process model for welding simulation of double-sided fillet welds with single weld passes is verified. The verified parameters for double-sided fillet welds with single weld passes are validated using an extended set of parameters in the case of a multi-pass welded double-bevel butt weld, double-sided fillet weld, and single-bevel butt weld. A three-dimensional heat transfer model is used to predict the weld pool size in fillet and butt weld configurations during metal active gas welding with fair precision in S355 structural steel weldments using a mixture of pure argon and carbon dioxide as shielding gas, PA flat or PB horizontal-vertical welding positions, and two different electrode types. The approach is implemented in the finite element code for further parametric studies and the sustainable virtual manufacturing of stator segments of a wind turbine as a final application in the future.

Funding information Open access funding provided by Budapest University of Technology and Economics (BME). The presented research program received funding from Hungarian R&D project under grant agreement no. GINOP-2.1.1-15-2016-008854. The second author of the paper was supported by the ÚNKP-18-4 New National Excellence Program of the Ministry of Human Capacities and by the János Bolyai Research Scholarship of the Hungarian Academy of Sciences.

References

1. Lindgren LE (2001) Finite element modeling and simulation of welding part I: increased complexity. J Therm Stresses 24:141–192
2. Goldak JA, Akhlaghi M (2005) Computational welding mechanics. Springer Science + Business Media, Inc., Boston
3. L.E. Lindgren (2007) Computational welding mechanics: thermomechanical and microstructural simulations, Cambridge, Woodhead Publishing. https://www.worldcat.org/title/computational-welding-mechanics-thermomechanical-and-microstructural-simulations/oclc/906243187&referer=brief_results
4. Kik T, Slovacek M, Vanek M (2015) Use of welding process numerical analyses as technical support in industry. Part 3: industrial examples – transport industry. Biuletyn In¬stytutu Spawalnictwa 6: 38–45
5. Brust FW, Scott P (2007) Weld distortion control methods and applications of weld modeling. In: Transactions of the 19th International Conference on Structural Mechanics in Reactor Technology, Toronto, August 2007, paper #B05/1
6. Kollár D, Kövesdi B (2016) Experimental and numerical simulation of welded columns. In: Bauer B, Garasic I (eds) Proceedings of 41st International Conference Zavarivanje – Welding 2016 - Opatija, Croatia, Hrvatsko Drustvo Za Tehniku Zavarivanja/ Croatian Welding Society, Zagreb, ISBN 978-953-7518-04-2, Opatija, Croatia, 8-11 June 2016, pp 123–132
7. Kollár D, Kövesdi B, Néző J (2017) Numerical simulation of welding process – application in buckling analysis. Period Polytech Civ Eng 61:98–109. https://doi.org/10.3311/PPci.9257
8. Kollár D, Kövesdi B (2018) Effect of imperfections and residual stresses on the shear buckling strength of corrugated web girders. In: Camotim D, Silvestre N (eds) Proceedings of the Eighth International Conference on Thin Walled Structures, Lisbon, Portugal, 24–27 July 2018 p 20
9. EN 1993-1-5:2006 (2006) Eurocode 3: Design of steel structures. Part 1-5: Plated structural elements. European Committee for Standardization (CEN); 2006
10. Sudnik W, Radaj D, Breitschwerdt S, Erofeew W (2000) Numerical simulation of weld pool geometry in laser beam welding. J Phys D Appl Phys 33:662–671

11. Sudnik W, Radaj D, Erofeew W (1998) Computerized simulation of laser beam weld formation comprising joint gaps. J Phys D Appl Phys 31:3475–3480
12. Lundback A (2003) Finite element modelling and simulation of welding of aerospace components. PhD. Lulea University of Technology. https://www.worldcat.org/title/finite-element-modelling-and-simulation-of-welding-of-aerospace-components/oclc/1026798793&referer=brief_results
13. Rosenthal D (1946) The theory of moving sources of heat and its application to metal treatments. Trans ASME 48:848–866
14. R.R. Rykalin (1951) Calculations of thermal processes in welding (in Russian), Moscow. https://www.worldcat.org/title/rascety-teplovych-processov-pri-svarke/oclc/253053446&referer=brief_results
15. Goldak JA, Oddy A, Gum M, Ma W, Mashaie A, Hughes E (1992) Coupling heat transfer, microstructure evolution and thermal stress analysis in weld mechanics. In: Karlsson L, Lindgren L-E, Jonsson M (eds) Mechanical effects of welding. International Union of Theoretical and Applied Mechanics, Springer, Berlin, pp 1–30
16. Nguyen NT (2004) Thermal analysis of welds. WIT Press, Southampton
17. Pavelic V, Tanbakuchi R, Uyehara OA, Myers PS (1969) Experimental and computed temperature histories in gas tungsten-arc welding of thin plates. Weld J 48:295s–305s
18. Rykalin RR (1974) Energy sources for welding. Weld World 12: 227–248
19. Néző J (2011) Virtual fabrication of full size welded steel plate girder specimens. University School of Enginering and Physical Science. https://www.worldcat.org/title/virtual-fabrication-of-full-size-welded-steel-plate-girder-specimens/oclc/857998501&referer=brief_results
20. Gu M, Goldak JA, Hughes E (1993) Steady state thermal analysis of welds with filler metal addition. Can Metall 32:49–55
21. Goldak JA, Chakravarti A, Bibby M (1984) A new finite element model for welding heat sources. Metall Trans B 15:299–305
22. Chukkan JR, Vasudevan M, Muthukumaran S, Kumar RR, Chandrasekhar N (2015) Simulation of laser butt welding of AISI 316L stainless steel sheet using various heat sources and experimental validation. J Mater Process Technol 219:48–59
23. Dal M, Fabbro R (2016) An overview of the state of art in laser welding simulation. Opt Laser Technol 78:2–14
24. Nguyen NT, Mai YW, Ohta A (2000) Analytical solution for a new hybrid double-ellipsoidal heat source in semi-infinite body. In: W.R.B. & W.P.D.W. C.A. Brebia (ed) Proceedings of International Conference on Advances in Composite Materials and Structures VII. WIT Pres, Bologna, pp 207–217
25. Thasanaraphan P (2012) A study on the welding characteristics of tailor welded blank metal sheets using GTAW and laser welding. Lehigh University, PhD dissertation. https://www.worldcat.org/title/study-on-the-welding-characteristics-of-tailor-welded-blank-metal-sheets-using-gtaw-and-laser-welding/oclc/895662707&referer=brief_results
26. ANSYS version 16.2 (2016). Computer software. ANSYS Inc., Canonsburg, Pennsylvania, USA
27. Radaj D (1992) Heat effects of welding: temperature field, residual stress, distortion. Berlin, Springer. https://doi.org/10.1007/978-3-642-48640-1
28. ANSYS version 17.2 (2016) Reference manual. ANSYS Inc., Canonsburg
29. Bradac J (2012) Using welding simulations to predict deformations and distortions of complex car body parts with more welds. Machines, Technologies, Materials 4:29–32
30. J.A. Goldak (2013) Web based simulation of welding and welded structures. http://www.ewp.rpi.edu/hartford/~ernesto/F2014/MPT/MaterialsforStudents/%0APatella/Goldak2013-web-based-simulation.pdf. Accessed 30 Aug 2017
31. Goldak JA, Patel B, Bibby M, Moore J (1986) Computational weld mechanics, AGARD Conference Proceedings, paper #398, pp 1–32
32. Lindgren LE, Runnemalm H, Nasstrom MO (1999) Simulation of multipass welding of a thick plate. Int J Numer Methods Eng 44: 1301–1316
33. Rhodin M (2012) Calculation of welding deformations in a pipe flange. Chalmers University of Technology. MSc thesis http://publications.lib.chalmers.se/records/fulltext/162770.pdf
34. Robertson J, A., Svedman (2013) Welding simulation of a gear wheel using FEM. Chalmers University of Technology. MSc thesis http://publications.lib.chalmers.se/records/fulltext/182423/182423.pdf
35. EN 1993-1-2:2005 (2005). Eurocode 3: Design of steel structures. Part 1-2: General rules – Structural fire design. European Committee for Standardization (CEN); 2005
36. Kollár D, Kövesdi B (2015) Numerical simulation of welding process. In: Young Welding Professionals International Conference, YPIC2015, Budapest, Hungary, 7–9 October 2015, p 6
37. Somodi B, Kollár D, Kövesdi B, Néző J, Dunai L (2017) Residual stresses in high-strength steel welded square box sections. Proc Inst Civ Eng Struct Build 170:804–812. https://doi.org/10.1680/jstbu.16.00139
38. EN 1011-1:2009 (n.d.). Welding - Recommendations for welding of metallic materials - Part 1: General guidance for arc welding